Postseismic deformation following the April 25, 2015 Gorkha earthquake (Nepal): Afterslip versus viscous relaxation

François Jouanne, Ananta Gajurel, Jean-louis Mugnier, Laurent Bollinger, Lok Bijaya Adhikari, Bharat Koirala, Nathalie Cotte, Roshanraj Bhattarai, Pascale Bascou, Pascale Huyghe

Postseismic deformation following the April 25, 2015 Gorkha earthquake (Nepal): afterslip versus viscous relaxation.

François Jouanne (1), Ananta Gajurel (2), Jean-Louis Mugnier (1), Laurent Bollinger (3), Lok Bijaya Adhikari (4), Bharat Koirala (4), Nathalie Cotte (1), Roshanraj Bhattarai (2,1), Arnaud Pecher (1), Pascale Bascou (1), Pascale Huyghe (1).

1Univ. Grenoble Alpes, Univ. Savoie Mont Blanc, CNRS, IRD, IFSTTAR, ISTerre.
2 Department of Geology, Tribhuvan University, Ghantaghar, Kathmandu, Nepal
3 CEA, DAM, DIF, Arpajon, France.
4 Department of Mines and Geology, National Seismological Center, Kathmandu, Nepal.

Abbreviated title suitable for page headings:
Postseismic deformation following the Gorkha earthquake.

Corresponding author:
François Jouanne,
Université de Savoie Mont Blanc, ISTerre,
F-73376 Le Bourget du Lac, France
Email : fjoua@univ-smb.fr
Tel : (33) 608371432

Abstract

The postseismic deformation consecutive to the April 25, 2015 Gorkha earthquake (Mw 7.9) is estimated in this paper based on a cGNSS network installed prior to the earthquake and supplemented by 6 cGNSS stations installed after the main shock. Postseismic displacement are obtained from daily time series corrected for interseismic deformation and seasonal variations. The maximum postseismic displacement is found north of the rupture area, where locally it reached 100 mm between the date of the earthquake and late 2016. The postseismic deformation affects the northern part of the rupture area but not the southern part, along the

southern part of the Main Himalayan Thrust (MHT). Three hypotheses for the mechanisms controlling postseismic deformation are tested through numerical simulations of the postseismic time series: (i) viscous relaxation, (ii) afterslip, or (iii) a combination of these two mechanisms. We can exclude postseismic deformation controlled by viscous relaxation of a thick deformation zone along the northern and lower flat of the MHT. However, it is impossible to discriminate between postseismic deformation controlled by either afterslip along the MHT (northern part of the rupture zone, crustal ramp, and lower flat of the MHT) or a combination of afterslip along the MHT (northern part of the rupture zone, crustal ramp) and viscous relaxation controlled by a thin (~3-4 km thick) low-viscosity body centered on the lower flat of the MHT. The occurrence of afterslip along the northern part of the upper flat of the MHT and its longitudinal variations have been established thanks to the densification of GNSS network by our team presented in this paper.

Introduction.

The large number of geophysical instruments which recorded the April 25, 2015 Mw 7.8 Gorkha earthquake provides a unique opportunity to document better than ever a large Himalayan earthquake. The main instrumental contributors to our understanding of the mainshock include Interferometric synthetic aperture radar (InSAR) investigations as well as teleseismic data (e.g. Avouac et al., 2015, Fan and Shearer, 2015), with also the continuous Global Navigation Satellite System (GNSS) time series (Grandin et al., 2015) and regional seismological records (e.g.Adhikari et al., 2015; Baillard et al., 2017). The deployment of the Nepal GPS Geodetic Network, prior to the earthquake, and its maintenance during the seismic crisis has also allowed to quantifying the early postseismic surface deformation (KKN4 and CHLM stations) consecutive to this large earthquake (Mencin et al., 2016; Gualandi et al., 2016).

In addition to being one of the few instrumental Himalayan earthquake, the setting of the 2015 earthquake (Fig. 1&2) is appropriate to study the complexity of the seismic cycle in a continental subduction zone. Indeed, the slip deficit along the main Himalayan thrust (MHT), on which the mainshock occurred, is accommodated during various types of earthquakes (Mugnier et al., 2013), that partially contributes to release the elastic strain accumulation (Avouac et al., 2015). This partial release has already been instrumentally measured in several oceanic subduction environments; for example, in the Andean convergent margin, the main slip patch of the 2010 Mw 8.8 earthquake occurred in an area that was highly coupled and had already released slip in 1960 (Melnick et al., 2012; Moreno et al., 2012). However, contrarily to earthquakes ruptures at oceanic subduction zones rarely captured by GNSS network in their whole extend due to their frequent extension offshore, the 2015 Gorkha rupture was surrounded by 12 stations well distributed above and around it. In addition, this permanent network was complemented during the weeks following the main shock, by the deployment of additional permanent or semi-permanent GNSS stations (this paper), this network dedicated to the postseismic deformation has been designed to test the occurrence of afterslip along the upper flat of the MHT in the rupture zone and south of it.

These records add some details to the postseismic deformation pattern and give a unique opportunity to study in greater details the mechanism controlling the postseismic deformation associated with the 2015 Gorkha event.

Different mechanisms are usually inferred for the postseismic deformation: afterslip or viscous relaxation. In this paper, the Relax software (Barbot et al., 2009) was used to model the postseismic deformation, taking into account the Main Himalayan Thrust geometry, rather well imaged in the region (Nabelek et al., 2009; Duputel et al., 2016) and the coseismic displacement field associated to it. Three postseismic mechanisms were tested: afterslip, viscous relaxation or a combination of these two phenomena. We used a flap-ramp-flat geometry (Elliott et al.,

2016) with a southern and upper flat corresponding to the geometry adopted by Grandin et al. (2015) to describe the coseismic slip distribution of the Gorkha earthquake along this flat.

Geological setting.

The structure of the Himalaya results from the underthrusting of the Indian lithosphere along the Main Himalayan Thrust (MHT) beneath the Tibetan Plateau (Argand, 1924). Great earthquakes have episodically ruptured segments of the brittle upper part of the MHT (e.g. Avouac et al., 2001; Mugnier et al., 2013, Bollinger et al., 2014). The Nepal earthquake of April 25, 2015 followed a series of great earthquakes in the Central Himalaya (Mugnier et al., 2011, Bollinger et al., 2016): over the last two centuries, the city of Kathmandu was severely damaged in 1833, 1866, and 1934.

The April 25, 2015 event (Fig. 1) was the first earthquake on the MHT to be simultaneously recorded by numerous instruments: high-rate GPS (e.g. Avouac et al., 2015), teleseismic waves (e.g. Fan and Shearer, 2015), SAR imaging (e.g. Lindsey et al., 2015), InSAR and teleseismic waves (Grandin et al., 2015), strong-motion recordings (e.g. Bhattarai et al., 2015), and a local seismometer network (Adhikari et al., 2015).

The rupture was mainly located to the NW of Kathmandu, at a depth of 13–15 km on a flat portion of the Main Himalayan Thrust (MHT) that dips N–NE at 7–10°. The northern boundary of the main rupture corresponds to the transition towards a steeper crustal ramp. This ramp, which is partly coupled during the interseismic period (Jouanne et al., 2017), was only locally affected by the earthquake (Elliott et al., 2016). The southern boundary of the rupture was near the leading edge of the Lesser Himalaya antiformal duplex (Mugnier et al., 2017) and possibly near the frontal footwall ramp of the upper Nawakot duplex (Hubbard et al., 2016). This rupture was affected by transversal structures: on the western side, a ~20° dipping lateral ramp (Kumar et al., 2017), located beneath the Judi lineament (Mugnier et al., 2017) and already defined by

Kayal (2008), separates the main rupture zone from the nucleation area. On the eastern side, a lateral ramp (Mugnier et al., 2017) located beneath the Gaurishankar lineament (Kayal, 2008) illustrated by its seismic signature at depth (Letort et al., 2016, Baillard et al., 2017) separates the April 25, 2015 rupture from the May 12, 2015 (Mw 7.2) rupture.

Data acquisition and analysis.

After the April 25 Gorkha earthquake, we installed a GNSS network designed to record postseismic deformation induced by this Mw 7.9 earthquake. We installed four permanent GNSS stations in June 2015 and 11 campaign GNSS stations between June and December 2015. Seven of these stations were measured again in November 2016 (Figs 3 and 4). We analyzed these data together with the continuous GNSS networks established by LDG-DASE, Caltech (www.unavco.org), Central Washington University (http://www.geodesy.cwu.edu) and with data from the GNSS sites defined in the ITRF2014 reference frame (Altamimi et al., 2016) (ARTU, BADG,BAKU,BJFS, BJNM, CHUM, CUSV, GUAO, HYDE, IISC, IRKJ, IRKM, KIT3, KUWT, LHAZ, MDVJ, POL2, SGOC, SHAO, TALA, TASH, TCMS, TEHN, TNML, URUM, ZECK) obtained from unavco.

The data were analyzed using Bernese 5.2 software (Dach et al., 2016) with absolute antenna phase center offset models, together with precise IGS orbits, Earth rotation parameters, and ocean tidal loading and atmospheric tidal loading estimates. Velocities and time series were estimated in the ITRF2014 reference frame (Altamimi et al., 2016) with discontinuities associated with this reference frame and expressed in terms of the India fixed reference frame by the use of the rotation pole proposed by Ader et al. (2012). This rotation pole, originally proposed to describe the motion of India relative to ITRF2005, accurately describes the India plate motion in the ITRF2014 reference frame, as shown by Jouanne et al. (2017) and as

exemplified by the lack of velocity of the cGPS SIM4 station located on the India plate (Fig. 3). In any case, any velocity changes introduced by the ITRF2005 / ITRF2014 change are negligible compared to the large postseismic displacements.

We followed the resolution strategy with (1) an initial ionosphere-free analysis with calculation of the residuals; (2) a residual analysis; (3) code-based wide-lane ambiguity resolution for all baselines (Melbourne, 1985; Wübbena, 1985), using differential code bias (DCB) files when available and calculation of the ionosphere-free solution with the introduction of resolved Melbourne-Wübbena linear combination ambiguities; (4) phase-based wide-lane (L5) ambiguity resolution for baselines < 200 km and computation of the ionosphere-free solution with the introduction of resolved ambiguities; (5) resolution of the previously unresolved ambiguities for baselines < 2000 km using the quasi ionosphere-free strategy of resolution; (6) direct L1/L2 ambiguity resolution for baselines < 20 km with the introduction of an ionosphere model; (7) calculation of the normal equations; (8) a compatibility test between the daily free solution and ITRF2014 solution, selection of compatible ITRF2014 stations, and (9) transformation of the daily normal equation in the ITRF2014 reference frame with a six-parameter Helmert solution (three translation parameters and three rotation parameters) using the ITRF2014 selected stations. During these steps, site-specific troposphere parameters were estimated every two hours.

Normal equations were analyzed simultaneously to determine accurate velocities in the ITRF2014 reference frame with the introduction of ITRF2014 coordinates and velocities. Outliers and new discontinuities were detected using the “Find Outliers and Discontinuities in Time Series” tool in Bernese 5.2 software which estimates annual seasonal fluctuations and reduces, step by step, the discrepancy between the functional model and the time series due to statistical adjustment (Ostini et al., 2008). Bernese 5.2 software underestimates the daily errors because systematic errors or mismodeled parameters are not included in the formal error. We

157 therefore rescaled the formal errors by multiplying them by a factor of 10 to obtain a more
158 realistic estimated error (Hugentobler et al., 2001).
159
160 Results: postseismic displacements at the surface.
161
162 We consider that displacements contain three superimposed signals: interseismic
163 displacements, postseismic displacements, and the seasonal signal associated with loading of
164 the Ganga Plain during the monsoon and its unloading during the dry season (Bettinelli et al.,
165 2008; Fu and Freymueller, 2012; Gualandi et al., 2016). In order to analyze postseismic
166 displacements, we removed the interseismic displacements that were either measured before
167 the Gorkha earthquake for the sites that already existed before this event (BESI, BRN2, CHLM,
168 DAMA, GUMB, KKN4, KLDN, LMJG, NAST, ODRE, RMJT, RMTE, SNDL, SYBC, TPLJ)
169 (Fig. 2; Jouanne et al., 2017) or were estimated using interseismic deformation modeling by
170 Jouanne et al. (2017) for the new GNSS sites (Fig. 3).
171 In order to evaluate the seasonal components, we make the hypothesis that time series
172 are nearly linear during the period beginning 300 days after the 25 April 2015 earthquake. For
173 the period beginning 300 days after the main shock, we have then modeled time series as the
174 consequence of a linear velocity and of seasonal component (eq. 1).
175 $U(t) = U*(t-t_{ref}) + a \cos(2\pi*(t- t_{ref})/365) + b \sin(2\pi*(t- t_{ref})/365) + c \cos(2\pi*(t- t_{ref})/182.5) +$
176 $d \sin(2\pi*(t- t_{ref})/182.5)$ (eq. 1)
177 Where t_{ref} is the first date after the day D_0+300 existing in the time series, D_0 being the date of
178 the main shock, U the velocity, and a, b, c and d are the amplitude of annual and semi-annual
179 signals. In a second step, whole time series are corrected for seasonal signals using these
180 amplitudes.
181

182 The postseismic displacements for the period when most of the GNSS stations were
183 available (between June 24, 2015 and late 2016) are shown (Fig. 4) to compare site
184 displacement measured over the same time span. Postseismic displacements are characterized
185 by the southward displacements of the points north of the Gorkha rupture (CHLM, GUMB,
186 TSM1). The station that recorded the greatest postseismic displacement is CHLM (Fig. 4 and
187 5) located to the north of the rupture, with 40 mm of southward displacement between April 25
188 and June 24, 2015 and 100 mm of southward displacement between June 24, 2015 and late
189 2016. The points located in the northern part of the rupture zone (KKN4, GURJ, BALE) are
190 affected by moderate southward postseismic displacements, whereas the points located at the
191 southern end of the rupture, near to and south of Kathmandu (CHIR, DAMA,NAST and
192 XYAK), are subject to small postseismic displacement. It should be noted that the points at the
193 western part of the rupture (LMJG, GORK and ANBU) are not affected by postseismic
194 displacements whereas the points located several kilometers to the east of the April 25, 2015
195 rupture (CHAR, JIR2, MALU) are affected by significant postseismic displacements reaching
196 35 mm (Fig. 4). Given that these points were installed after the Mw 7.2 main aftershock of May
197 12, 2015, these postseismic displacements could be related to the postseismic deformation
198 induced by this earthquake, but the lack of change in the cumulative postseismic displacements
199 in the CHLM time series indicates, before and after the May 12, 2015 earthquake indicates that
200 this second large earthquake does not induce a significant postseismic deformation.
201 Significant postseismic displacements are therefore restricted to the northern part of the rupture
202 zone and to an area to the north of it (Figs 4, 5, 6 and 7). It is important to note that there are no
203 clear postseismic displacements to the south of the Gorkha earthquake rupture and, like Mencin
204 et al. (2016), we exclude the occurrence of significant afterslip along the southern part of the
205 MHT. Therefore, the slip deficit along the MHT south of Kathmandu is not resorbed
206 aseismically by slip along the MHT from the rupture zone to the MFT where the MHT emerges.

The slip deficit could then possibly be resorbed by a future large earthquake between the southern end of the rupture near Kathmandu and the Main Frontal Thrust near the Ganga Plain, as probably happened in the 1866 earthquake (Oldham, 1883; Szeliga et al., 2010), or by a larger earthquake rupturing the locked fault zone from the brittle-ductile transition zone to the surface, in a similar way as in the subduction zones (Melnick et al., 2012; Moreno et al., 2012) or to the 1934 Nepal-Bihar earthquake (e.g. Mugnier et al., 2013).

Figures 5, 6 and 7 illustrate the postseismic deformation with the time series for the southern, eastern and vertical components corrected for the interseismic component and the seasonal signal in the India fixed reference frame.

Time series of southern component present a progressive decrease in postseismic displacement with time, suggesting progressive dissipation of the stress perturbation induced by the earthquake (Fig. 5). It can be observed that the time series of the eastern components (Fig. 6) presents spatial variations: BALE, CHLM and DNC4 time series indicate significant westward components of postseismic displacements, whereas time series of BHAZ, CHAR, GUMB, JIR2, KKN4 and XBAR do not present this component. This is why we will consider only the southern and vertical time series to simulate postseismic displacements. Time series of vertical component present a progressive decrease in postseismic displacement with time, suggesting progressive dissipation of the stress perturbation induced by the earthquake (Fig. 7). The CHLM time series of the south components presents a jump corresponding to the Mw 7.2 main aftershocks of May 12, whereas the other stations were not significantly affected or were installed too late to record this coseismic displacement. It can be also observed that this second earthquake does not induced a change in the evolution of the postseismic displacement of the CHLM and KKN4 station. This is why we have not consider this earthquake in the numerical simulations.

232 Modeling postseismic- displacement.

233 We have chosen to test the origin of the progressive release using three hypotheses with
234 Relax 1.0.7 software (Barbot et al., 2008; Barbot et al., 2009; Barbot and Fialko 2010; Bruhat
235 et al., 2011; Rousset et al., 2012): a postseismic deformation controlled by afterslip, viscous
236 relaxation of the stress perturbation with a linear rheology, and a combination of these two
237 mechanisms.

238 This software computes the displacement and stress due to dislocations and the nonlinear
239 postseismic time-dependent deformation, the latter either controlled by viscous bodies or by
240 rate-strengthening friction faults. This software takes gravity into account and is based on a
241 Fourier-domain elastic Green's function and an equivalent body-force representation of
242 deformation mechanisms. We consider a 512*512*512 grid size model around the relevant
243 faults with 0.7*0.7*0.7 km sampling which corresponds at a 358*358*358 km grid.

244 For this modeling, we use the same MHT geometry as for the pre-earthquake
245 deformation (Jouanne et al., 2017); this geometry also fits with the location of the rupture zone
246 proposed by Grandin et al. (2015) indicated in Figure 2. The geometry of the MHT is formed
247 by a succession of flats and ramps characterized by a large southern flat (95–100 km) dipping
248 7° northward, a crustal ramp dipping 27° northward between 15 and 25 km, and a northern flat
249 dipping 7° northward as illustrated by receiver-function data (Duputel et al., 2016).

250 As postseismic displacements only affected stations north of Kathmandu, if postseismic
251 displacements are controlled by afterslip along the MHT, afterslip did not affect all of the upper
252 flat of the MHT but only its northern parts. If we consider the points BALE, KKN4, and GURJ
253 (Fig. 4 and 5) that are nearly the same distance from the upper flat-ramp connection, it appears
254 that the eastern one (BALE) is affected by greater postseismic displacements than the other two
255 located in the western part of the upper flat of the MHT. We then considered that these surficial
256 variations in displacement reflect afterslip distribution along the MHT. These spatial variations

in the time series led us to consider a 25 km-wide western segment and a 40 km-wide eastern segment and the boundary between these two segments coincides with the western edge of the May 12, 2015 rupture and with the Gaurishankar lateral ramp as illustrated in Figure 1. This spatial variation also reflects interseismic coupling variations between the western and eastern parts: the western part was completely locked whereas the eastern part was only partially locked, with a coupling of 0.7 (Fig. 2a) (Jouanne et al., 2017).

To test the models, we used a time series that was corrected for interseismic velocities and seasonal components. As postseismic displacements are southward with a lack of E-W components, we have only used the N-S and vertical components of time series.

The preferred solutions were selected using the comparison between the observed and simulated time series with the estimation of weighted root mean square WRMS for each simulation (Fig. 9).

Viscous relaxation model.

The estimation of coupling during the interseismic period (Betinelli et al., 2006; Ader et al., 2012; Jouanne et al., 2017) suggests ductile behavior along the northern flat of the MHT. We therefore test the hypothesis that postseismic displacements reveal viscous relaxation of the stress perturbation induced by the main shock. Ductile behavior is temperature dependent (Scholz, 1998) and does not occur in the brittle crust. Viscous relaxation is therefore excluded for the upper flat and the ramp characterized by a temperature of less than 375 °C (Robert et al., 2011). Hereafter, we assume that the lower flat accommodates viscous relaxation only.

In this simulation, a low viscous body with a linear Maxwell rheology corresponding to the deeper part of the Main Himalayan Thrust is embedded in an elastic half space (Fig. 8a). The parameters to be determined are the viscosity and the thickness of this body. As the indian

lithosphere is very thick, 135 km in eastern Nepal (Devi et al., 2011), we do not take into account the asthenosphere viscosity.

We chose to explore the following ranges of values: viscosity of the body from 10^{16} to 10^{19} Pa*s and thickness of the body from 0 to 14 km. The WRMS is invariably greater than 17 mm and no solution is clearly favored among the 84 numerical runs performed to determine parameter influence and summarized in Figure 9a.

Afterslip model.

If the postseismic displacements are controlled by afterslip induced by the Mw 7.9 earthquake of April 25 2015, these displacements can be simulated by progressive release of stress perturbation due to the main shock. We assume that the afterslip occurs (Fig. 8a) along the northern part of the upper flat of the MHT affected by the April 25, 2015 earthquake, along the crustal ramp north of the rupture zone, and along the lower flat north of this ramp.

We assign rate-strengthening properties derived from laboratory experiments (Dieterich, 1979; Ruina, 1983, Barbot et al., 2009; Lapusta et al., 2000; Rice & Ben-Zion, 1996) to these three fault segments with:

$$V = 2\,\dot{\gamma}_0 \sinh \frac{\Delta\tau}{(a-b)\sigma} \quad \text{(eq. 2)}$$

Where V is the slip velocity on the fault, $\Delta\tau$ is the shear stress perturbation induced by the earthquake that is progressively released by the afterslip, $\dot{\gamma}_0$ is the initial slip velocity and (a - b) σ is a constitutive parameters with a value of the order of the stress drop during the earthquake, σ being the effective normal stress and (a - b) a frictional parameter.

The initial stress perturbation associated with the coseismic slip distributions of April 25, 2015 estimated by Grandin et al. (2015), with InSAR and teleseismic waves data (Fig. 2b) is calculated with Relax 1.0.7 software.

We explore the parameters space (Fig. 9b, c, d) formed by $\dot{\gamma}_0$ (from 50 to 500 mm/year), and the friction along the relevant planes (from 0.2 to 0.7) for (a - b) σ values of 10 and 22 MPa (22 MPa being the stress drop estimated by Denolle et al., 2015). The tests of the (a - b) σ values of 22 and 10 MPa (Fig. 9 c and d) allow us to determine that the best fit fort the southern component time series is obtained for the (a - b) σ value of 22 MPa, which is the value of the stress drop estimated by Denolle et al. (2015), a friction ratio of 0.7 and a $\dot{\gamma}_0$ = 200 mm/year. The simulation of vertical time series allows to confirm that $\dot{\gamma}_0$ must be larger than 150 mm/year (Fig. 9d).

We decide to adopt as the better model the solution obtained for 0.7 frictional parameters and a $\dot{\gamma}_0$ value of 200 mm/year.

Afterslip and viscous relaxation model.

This simulation takes into account the hypothesis that the northern flat may be a zone affected by ductile deformation (Beaumont et al., 2001), while the upper part of the MHT is probably in a brittle condition as shown by the high coupling of the upper flat and crustal ramp during the interseismic period (Jouanne et al., 2004; Ader et al., 2012; Jouanne et al., 2017).

We test the hypothesis of a mixed origin for postseismic deformation (Fig. 8), with viscous relaxation controlled by a deep low-viscosity body centered on the northern MHT flat, as done above, whereas afterslip occurs along the crustal ramp and the northern part of the southern flat. We adopt, as an *a priori* model for the afterslip component, the above model that minimizes the WRMS among the models based solely on afterslip and we explore the following parameters: viscosity of the low-viscosity body (from 10^{16} to 10^{19} Pa.s) and the thickness of this body (1 to 6 km).

Among 50 numerical runs performed to determine the parameter influence with the southern time series (Figure 9e), a minimum of 3.2 mm is found for the WRMS (Fig. 9e) linked to a 3-4

330 km thickness for the viscous body and a 10^{16} Pa*s viscosity. The used of vertical component to
331 determine the best solution (Fig. 9 e) is not determining.
332
333 Discussion.
334 *Comparison between the different models.*
335 Comparison of the WRMS for the models performed with the three hypotheses tested
336 (Fig. 9) indicates that the models with only viscous relaxation on the lower flat of the MHT
337 have much higher WRMS and can be excluded (Fig. 9a).
338 The other two models, afterslip alone or afterslip associated with viscous relaxation on the
339 lower flat of the MHT, have respectively WRMS for the southern time series of 3.6 mm for the
340 afterslip model and of 3.2 mm for the mixed model. The use of vertical time series (Fig. 9d and
341 9f) do not help to choose between these two models.
342 The mixed model seems to better simulate the observations than the afterslip only model, but
343 if the Relax software allowed the use of variable friction coefficients along the MHT, it would
344 probably be possible to find a more satisfactory solution with the afterslip model, with probably
345 a lower friction coefficient along the northern flat of the MHT than along the ramp and the
346 southern or upper flat of the MHT.
347 Therefore the numerical modeling approach does not enable us to choose between the two
348 hypotheses – afterslip alone or afterslip combined with viscous relaxation on the lower flat (Fig.
349 9c and 9e and Fig. 10). Nevertheless, it must be underlined that afterslip combined with viscous
350 relaxation on the lower flat allows to simulate the early postseismic displacements as shown on
351 Figure 10 for the CHLM and KKN4 time series which is not the case if we consider the afterslip
352 only model.
353 All the retained simulations indicate (Fig. 9c and d, Fig. 9 e and f, Fig. 11 and 12): (a) moderate
354 afterslip along the ramp; (b) significant afterslip along the northern part of the upper flat; (c)

355 substantial afterslip where the coseismic slip gradient was high: at the upper flat/crustal ramp
356 transition, locally in the rupture area, and near the southern boundary of the rupture. Afterslip
357 along the southern part of the upper flat, to the south of the southern border of the numerical
358 model, has been a priori excluded in our modelling as it has suggested by the near zero
359 postseismic displacement measured in the southern part of the Gorkha earthquake rupture zone.
360 This observation indicates the likely existence of local variations in friction coefficients not
361 taken into account in our model.
362
363 *Afterslip properties along the MHT.*
364 With Relax software it is possible to consider just one single afterslip property (friction
365 ratio and constitutive parameters) for all of the fault segments. As a result, we then considered
366 the same properties for the upper flat, crustal ramp, and lower flat of the MHT. Our preferred
367 model, which provides a good fit with the observed time series (Fig. 7c), was obtained with $\dot{\gamma}_0$
368 = 200 mm/year and a friction of 0.7 for (a-b) σ = 22 Mpa.
369 A friction coefficient of 0.7 is somewhat higher than the values usually inferred. For
370 example, the friction angle was estimated at 20° for the Indian crust in modeling by Berger et
371 al. (2003). Such high values have nonetheless been found experimentally for numerous rocks
372 (Kulhawi, 1975).
373 The afterslip evolution over time and space of our preferred model indicates that (Fig.
374 11): the lower flat of the MHT is affected by slow large-scale afterslip decreasing over time,
375 whereas the crustal ramp is affected by negligible afterslip without significant lateral variations.
376 The northern part of the upper flat is characterized by local patches of high afterslip; the latter
377 reached 1 m after two years with significant lateral variability and a significant decrease of
378 afterslip evolution between D + 30 days and D + 6 months. The areas of the upper flat affected
379 by significant slip are located close to the flat-ramp transition corresponding to the northern

boundary of the rupture. Areas of the upper flat locally affected by significant slip are characterized by a local high coseismic displacement gradient in Grandin et al.'s model (2016) and then by local high deviatoric stress to be released. Locally, slip also occurred southward, in areas near the southern end of the mesh, the upper flat segment of the MHT affected by afterslip. Our modeling suggests changes of width of the upper flat of the MHT affected by afterslip (Fig. 11). The distribution of the afterslip reflects the distribution of the coseismic displacement model, the roughness of the afterslip distribution reflects the roughness of the co-seimic displacement model considered at the input of the model. It can therefore be assumed that with a smoother coseismic displacement model, we would also obtain a smoother afterslip model. But we assume that the model roughness considered as input does not affect the conclusions of our models.

Our modelling clearly differs from the model proposed by Wang and Fialko, 2018, we allow afterslip along the northern part of the 2015 rupture whereas these authors supposed that no afterslip occurred along the upper flat of the MHT. Our model allows good simulation of time series of points located in the southern part of the area affected by postseismic deformation BALE, BHAZ, GURJ, KKN4, JIR2 and CHAR whereas the model of Wang and Fialko does not allow a good simulation of the time series of JIR2, the points BALE, BHAZ, GURJ and CHAR, installed by our team, being not included in their study. On the contrary, the model of Wang and Fialko presents a better simulation of the CHLM and DCN4 time series. Our model failed to predict accurately the early postseismic deformation of CHLM and failed to well fit the time series of DCN4 and GUMB. We can then propose that rheological properties are different between the upper flat of the MHT and the crustal ramp and the northern flat. As in this study we present a larger number of time series sensitive to the afterslip along the upper flat, we can suppose that our solution reflects mainly the rheological properties of the upper flat

whereas the results presented by Wang and Fialko, 2018 reflect mainly the rheological properties along the lower part of the MHT (ramp and northern flat).

Viscous relaxation controlled by a low viscosity zone along the lower flat of the MHT.

The time series for the stations located above the rupture zone, or to the south of it, are not correctly simulated by only viscous relaxation controlled by a ductile body centered on the northern flat. In the numerical models where afterslip along the upper flat of the MHT and along the crustal ramp has been introduced, the low-viscosity body (10^{16} Pa.s) has to be thin (close to 3-4 km) to minimize the discard between model and data (Fig. 9e). We therefore believe that viscous relaxation controlled by a low-viscosity body cannot alone explain the recorded postseismic deformation and another source of deformation located to the south of the lower flat (i.e. afterslip) is needed. Models combining afterslip and viscous relaxation controlled by a thin, viscous body centered on the lower flat of the MHT better predict early post-seismic displacement (CHLM and KKN4 time series) than models considering only afterslip along the MHT (Fig. 10).

The low-viscosity body is a reasonable assumption as it may explain the low coupling along the lower flat documented for the interseismic period (Fig. 2a and 12). Furthermore, the low-viscosity level has been suggested from the interpretation of deep images of the Himalayan crust (e.g. Zhao et al., 1993; Nelson et al., 1996). Since these articles, new seismic experiments demonstrated that the low velocity zones in Tibet is discontinuous, restricted to surfaces with maximum vertical extension of 10 km and maximum horizontal length about 50 km (Hetenyi et al., 2011).

A channel flow model (Beaumont et al., 2001) was even proposed to describe the evolution of Himalayan tectonics and is based on a very thick ductile zone (more than 10 km thick); so thick

429 that the horizontal velocity depicts a peculiar gradient, with a maximum velocity in the center
430 of the ductile zone. Our results nonetheless suggest that the ductile zone is 3 – 4 km thick
431 beneath the extreme southern part of the Tibetan plateau. Therefore, we suggest that the recent
432 tectonism of the Himalaya is not controlled by channel flow deformation at depth, although our
433 results does not preclude a thicker ductile zone to the north.
434
435 If we assume that postseismic deformation ends after 6 years, our results (Fig. 12) show (1)
436 afterslip or viscous relaxation of a thin body (~3-4 km thick) of low viscosity along the lower
437 flat of the MHT (up to 0.5 m after 6 years) and (2) moderate afterslip along the crustal ramp
438 that extends down-dip from the Gorkha rupture (up to 0.5 m after 6 years) as well as (3) a high-
439 velocity small-scale afterslip (up to 5 m after 6 years for the western segment) along the
440 southern boundary of the upper flat affected by afterslip, and along the upper flat, high-velocity
441 afterslip in areas characterized by a significant coseismic slip gradient during the earthquake
442 (reaching 5.6 m after 6 years in its western part and 3.4 m in its eastern part).
443 This pattern, in which moderate afterslip occurs along the crustal ramp and extends down-dip
444 from the rupture, has also been shown for the postseismic deformation following the 2005
445 Balakot-Bagh earthquake (Jouanne et al., 2011; Wang and Fialko, 2014), for the deformation
446 consecutive to the 1995 Chi-Chi earthquake (Yu et al., 2003; Perfettini and Avouac, 2004), and
447 for the 1995 Jalisco earthquake (Hutton et al., 2001).
448
449 *Importance of afterslip in the seismic cycle.*
450
451 As illustrated in Figure 12, the effects of afterslip consecutive to the Gorkha earthquake remain
452 confined to the northern part of the rupture area, the crustal ramp, and the northern flat of the
453 MHT. The afterslip does not, then, homogenize coseismic slips throughout the rupture area but

454 only and partially in its northern part. Moreover, if we consider that the 1833 and 2015
455 earthquakes have the same rupture area, and if we take the cumulated slip along the MHT during
456 the interseismic period as estimated by Jouanne et al. (2017), then it appears that postseismic
457 displacement along the MHT does not homogenize slip along the MHT between the ductile slip
458 along the northern flat (4 m for 200 years) and the coseismic slip along the northern part of the
459 upper flat.
460
461 Conclusion.
462 The cumulative postseismic velocity field clearly shows a lack of displacements to the
463 south of Kathmandu. Afterslip along the southern part of the rupture area of the Gorkha
464 earthquake and along the southern segment of the MHT, that was unaffected by the main shock,
465 is then clearly excluded. The slip deficit along the southern part of the upper flat of the MHT,
466 between Kathmandu and the Ganga Plain, would probably be transferred along the MHT by an
467 earthquake of large magnitude, as may have been the case after the previous 1833 large
468 earthquake along this segment of the MHT, or by a very large magnitude earthquake affecting
469 the MHT from the ductile zone to the MFT. To the west and east of the Gorkha rupture,
470 postseismic displacements are almost negligible, and afterslip does not affect the upper flat
471 areas of the MHT to the west of the rupture zone.
472 The simulation of the time series using Relax software suggests that the postseismic
473 deformation consecutive to the April 25, 2015 earthquake is controlled by: heterogeneous
474 afterslip along the northern part of the upper flat of the MHT corresponding to the northern part
475 of the rupture; afterslip along the crustal ramp reaching 0.17m after two years; and afterslip
476 reaching 0.20 m after two years or viscous relaxation of a thin (~3-4 km thick) ductile zone
477 along the lower flat of the MHT. Viscous relaxation along a ductile body centered on the lower
478 flat of the MHT alone cannot explain alone the postseismic deformation.

Acknowledgments.

The figures and maps were prepared using Generic Mapping Tools software (Wessel and Smith, 1995) and Paraview software (Ahrens et al., 2005; Ayachit, 2015). This material is partially based on data provided by the Nepal permanent GNSS network (DMG, Caltech, DASE) and data services provided by the UNAVCO Facility with support from the National Science Foundation (NSF) and National Aeronautics and Space Administration (NASA) under NSF Cooperative Agreement No. EAR-0735156. Funding was from the Labex OSUG@2020, INSU-CNRS, the AAP of Savoie Mont Blanc University, the IRD, and the ANR Bhoutanepal. We thank two anonymous reviewers for their detailed and constructive reviews.

References

Ader, T., Avouac, J.P., Liu-Zeng, J., Lyon-Caen, H., Bollinger, L., Galetzka, J., Genrich, J., Thomas, M., Chanard, K., Sapkota, S., Rajaure, S., Shrestha, P., Ding, L., Flouzat, M., 2012. Convergence rate across the Nepal Himalaya and interseismic coupling on the Main Himalayan Thrust: implications. *J. Geophys. Res*. 117, B04403. http://dx.doi.org/10.1029/2011JB009071.

Adhikari, L.B., Gautam, U.P., Bhattarai, M., Kandel, T., Gupta, R.M., Timsina, C., Maharjan, N., Maharjan K., Dahal, T., Hoste-Colomer, R., Cano, Y., Dandine, M., Guilhem, A., Merrer, S., Roudil, P., Bollinger, L., 2015. The aftershock sequence of the April 25 2015 Gorkha-Nepal earthquake. *Geophys. J. Int.* 203, 2119–2124.

Ahrens, J., Geveci, B., Law, C., 2005. *ParaView: An End-User Tool for Large Data Visualization*, Visualization Handbook, Elsevier, ISBN-13: 978-0123875822.

Ayachit, U., 2015. *The ParaView Guide: A Parallel Visualization Application*, Kitware, ISBN 978-1930934306.

Altamimi, Z., Rebischung, P., Métivier, L., Xavier, C., 2016. ITRF2014: A new release of the International Terrestrial Reference Frame modeling nonlinear station motions, *J. Geophys. Res. Solid Earth*, 121, doi:10.1002/2016JB013098.

Argand, E., 1924. La tectonique de l'Asie. 104 p. Compte rendu du congrès géologique international (1922). Vaillant-Carmane press (Liege, Belgium).

Avouac, J.P., Bollinger, L., Lavé, J., Cattin, R., Flouzat, M., 2001. Le cycle sismique en Himalaya, Comptes Rendus de l'Académie de Sciences - Serie IIa : Sciences de la Terre et des Planètes. doi:10.1016/S1251-8050(01)01573-7.

Avouac, J.-P., Meng, L., Wei, S., Wang, T., Ampuero, J.P., 2015. Lower edge of locked Main Himalayan Thrust unzipped by the 2015 Gorkha earthquake. *Nature Geoscience,* ISSN 1752-0894.

Baillard, C., Lyon-Caen, H., Bollinger, L., Rietbrock, A., Letort, J., Adhikari, L.B., 2017. Automatic analysis of the Gorkha earthquake aftershock sequence: evidences of structurally segmented seismicity. *Geophysical Journal International*, *209*(2), 1111-1125.

Barbot, S., Hamiel, Y., Fialko, Y., 2008. Space geodetic investigation of the coseismic and postseismic deformation due to the 2003 Mw 7.2 Altai earthquake: Implications for the local lithospheric rheology. *J. Geophys. Res.*, 113(B03403), doi:10.1029/2007JB005063.

Barbot, S., Fialko, Y., Bock, Y., 2009. Postseismic deformation due to the Mw 6.0 2004 Parkfield earthquake: stress-driven creep on a fault with spatially variable rate-and-state friction parameters. *J. Geophys. Res.*, 114(B07405), doi:10.1029/2008JB005748.

Barbot, S., Fialko Y., 2010. A unified continuum representation of postseismic relaxation mechanisms: semianalytic models of afterslip, poroelastic rebound and viscoelastic flow. *Geophys. J. Int.*, 182(3), 1124–1140, doi:10.1111/j.1365-246X.2010.04678.x.

Barbot, S., Fialko, Y., 2010. Fourier-domain Green's function for an elastic semi-infinite solid under gravity, with applications to earthquake and volcano deformation. *Geophys. J. Int.*, 182(2), 568–582, doi:10.1111/j.1365- 246X.2010.04655.x.

Beaumont, C., Jamieson, R.A., Nguyen, M.H., Lee, B., 2001. Himalayan tectonics explained by extrusion of a low-viscosity crustal channel coupled to focused surface denudation. *Nature* 414, 738–742.

Bettinelli, P., Avouac, J.-P., Flouzat, M., Bollinger, L., Ramillien, G., Rajaure, S., Sapkota, S., 2008. Seasonal variations of seismicity and geodetic strain in the Himalaya induced by surface hydrology. *Earth Planet. Sci. Lett.* 266, 332–344.

Berger, A., Jouanne, F., Hassani, R., Mugnier, J.L., 2004. Modelling the spatial distribution of present-day deformation in Nepal: how cylindrical is the Main Himalayan Thrust in Nepal? *Geophys. J. Int.*, 156, 94–114.

Bhattarai, M., Adhikari, L.B., Gautam, U.P., Laurendeau, A., Labonne, C., Hoste-Colomer, R., Hernandez, B., 2015. Overview of the large 25 April 2015 Gorkha, Nepal, earthquake from accelerometric perspectives. *Seismological Research Letters*, *86*(6), 1540-1548.

Bollinger, L., Sapkota, S.N., Tapponnier, P., Klinger, Y., Rizza, M., Van der Woerd, J., Tiwari, D.R., Pandey, R., Bitri, A., Bes de Berc, S., 2014. Estimating the return times of great Himalayan earthquakes in eastern Nepal: Evidence from the Patu and Bardibas strands of the Main Frontal Thrust, *J. Geophys. Res. Solid Earth*, 119, doi:10.1002/2014JB010970.

Bollinger, L., Tapponnier, P., Sapkota, S.N., Klinger, Y., 2016. Slip deficit in central Nepal: Omen for a repeat of the 1344AD earthquake ? Earth, Planets and Space, 68, 1-12, DOI 10.1186/s40623-016-0389-1.

Bruhat L., Barbot S., Avouac J.P., 2011. Evidence for postseismic deformation of the lower crust following the 2004 Mw 6.0 Parkfield earthquake. *J. Geophys. Res. Solid Earth*, 116 (B8).

Dach, R., S. Lutz, P. Walser, P. Fridez (Eds); 2015: **Bernese GNSS Software Version 5.2.** User manual, Astronomical Institute, University of Bern, Bern Open Publishing. DOI: 10.7892/boris.72297; ISBN: 978-3-906813-05-9.

Denolle, M.A., Fan, W., and Shearer, P.M., 2015. Dynamics of the 2015 M7.8 Nepal earthquake. *Geophys. Res. Lett.*, 42, 7467–7475, doi:10.1002/2015GL065336.

Devi E. Uma, Kumar P. and KumarM. Ravi, 2011,Imaging the Indian lithosphere beneath the Eastern Himalayan region ,*Geophysical Journal International*, Volume 187, Issue 2, 1 November 2011, Pages 631–641,https://doi.org/10.1111/j.1365-246X.2011.05185.x

Dieterich, J.H., 1979. Modeling of rock friction: 1. Experimental results and constitutive equations. *J. Geophys. Res.*, 84, 2161-2168.

Duputel, Z., Vergne, J., Rivera, L., Wittlinger, G., Farra, V., Hetényi, G., 2016. The 2015 Gorkha earthquake: a large event illuminating the Main Himalayan Thrust fault. *Geophys. Res. Lett.* 43 (2517–2525), 2016G. http://dx.doi.org/10.1002/L068083.

Elliott, J., Jolivet, R., Gonzalez, P., Avouac, J.P., Hollingsworth, J., Searle, M.P., Stevens, V.L., 2016. Himalayan megathrust geometry and relation to topography revealed by the Gorkha earthquake. *Nature Geosci.* http://dx.doi.org/10.1038/NGEO2623.

Fan, W., Shearer, P.M., 2015. Detailed rupture imaging of the 25 April 2015 Nepal earthquake using teleseismic P waves. *Geophys. Res. Lett.* doi:10.1002/2015GL064587.

Fu, Y., Freymueller, J.T., 2012. Seasonal and long-term vertical deformation in the Nepal Himalaya constrained by GPS and GRACE measurements. *J. Geophys. Res.* 117, B03407. doi:10.1029/2011JB008925.

Grandin, R., Vallée, M., Satriano, C., Lacassin, R., Klinger, Y., Simoes, M., Bollinger, L., 2015. Rupture process of the Mw = 7.9 2015 Gorkha earthquake (Nepal): http://dx.doi.org/10.1016/j.jseaes.2016.05.028 insights into Himalayan megathrust segmentation. *Geophys. Res. Lett.* 42 (20), 8373–8382.

Gualandi, A., Avouac, J.P., Galetzka, J., Genrich, J.F., Blewitt, G., Adhikari, L.B., Liu-Zeng, J., 2016. Pre-and postseismic deformation related to the 2015, Mw 7.8 Gorkha earthquake, Nepal. *Tectonophysics,* DOI: 10.1016/j.tecto.2016.06.014.

627

628 Hetényi, G., Vergne, J., Bollinger, L., & Cattin, R. (2011). Discontinuous low-velocity zones
629 in southern Tibet question the viability of the channel flow model. *Geological Society, London,*
630 *Special Publications*, *353*(1), 99-108.
631
632 Hubbard, J., Almeida, R., Foster, A., Sapkota, S.N., Bürgi, P., Tapponnier, P., 2016. Structural
633 segmentation controlled the 2015 Mw 7.8 Gorkha earthquake rupture in Nepal. *Geology*, *44*(8),
634 639-642.
635
636 Hugentobler U., Schaer S., Fridez, P., Bernese GPS Software Version 4.2. Astronomical
637 Institute, University of Berne, Switzerland, 2001.
638
639 Hutton, W., DeMets, C., Sánchez, O., Suárez, G., Stock, J., 2001. Slip dynamics during and
640 after the 9 October 1995 Mw = 8.0 Colima-Jalisco, Mexico. *Geophys. J. Int.*, 146, 637-658.
641 doi:10.1046/j.1365- 246X.2001.00472.x.
642
643 Jouanne, F., Mugnier, J.L., Gamond, J.F., Le Fort, P., Pandey, M., Bollinger, L., Flouzat, M.,
644 Avouac, J.P., 2004. Current shortening across the Himalayas of Nepal. *Geophys. J. Int.*,157, 1-
645 14.
646
647 Jouanne, F., Awan, A., Madji, A., Pêcher, A., Latif, M., Kausar, A., Mugnier, J.L., Khan, I.,
648 Khan, N.A., 2011. Postseismic deformation in Pakistan after the 8 October 2005 earthquake:
649 evidence of afterslip along a flat north of the Balakot-Bagh Thrust. *J. Geophys. Res.*, **116**,
650 B07401, doi:10.1029/2010JB007903.
651
652 Jouanne F., Mugnier J.L., Sapkota S.N., Bascou B., Pecher A., 2017. Estimation of coupling
653 along the Main Himalayan Thrust in the central Himalaya. *Journal of Asian Earth Sciences*,
654 January 2017.
655
656 Kayal, J.R., 2008. Microearthquake Seismology and Seismotectonics of South Asia.
657 http://dx.doi.org/10.1007/978-1-4020-8180-4.
658
659 Kulhawy F.H, 1975. Stress deformation properties of rock and rock discontinuities,
660 *Engineering Geology*, Volume 9, Issue 4, pp. 327-350.

661 Kumar A., Singh S.K., Mitra S., Priestley K.F., Shankar Dayal, 2017. The 2015 April 25
662 Gorkha (Nepal) earthquake and its aftershocks: implications for lateral heterogeneity on the
663 Main Himalayan Thrust. *Geophys. J. Int.*, 208 (2): 992-1008.
664
665 Lapusta, N., Rice, J., Ben-Zion, Y., & Zheng, G. (2000). Elastodynamic analysis for slow
666 tectonic loading with spontaneous rupture episodes on faults with rate- and state-dependent
667 friction. *Journal of Geophysical Research*, *105*(B10), 23,765–23,789.
668 https://doi.org/10.1029/2000JB900250.
669
670 Letort Jean, Laurent Bollinger, Helene Lyon-Caen, Aurélie Guilhem, Yoann Cano, Christian
671 Baillard, Lok Bijaya Adhikari; Teleseismic depth estimation of the 2015 Gorkha–Nepal
672 aftershocks, 2016, *Geophysical Journal International*, Volume 207, Issue 3, 1 December 2016,
673 Pages 1584–1595, https://doi.org/10.1093/gji/ggw364.
674
675 Lindsey, E.O., Natsuaki, R., Xu, X., Shimada, M., Hashimoto, M., Melgar, D., Sandwell, D.T.,
676 2015. Line-of-sight displacement from ALOS-2 interferometry: Mw 7.8 Gorkha Earthquake
677 and Mw 7.3 aftershock. *Geophysical Research Letters* 42, 6655-6661.
678 doi:10.1002/2015GL065385.
679
680 Melbourne, W.G., 1985. The case for ranging in GPS based geodetic systems. Paper Presented
681 at 1st International Symposium on Precise Positioning with the Global Positioning System, Int.
682 Assoc. of Geod., Rockville, Md.
683
684 Melnick, D., Moreno, M., Cisternas, M., Tassara, A., 2012. Darwin seismic gap closed by the
685 2010 Maule earthquake. *Andean Geology*, v. 39, no. 3, p. 558-563.
686
687 Mencin, D., Bendick, R., Upreti, B.N., Adhikari, D.P. Gajurel, A.P., Bhattarai, R.R.,
688 Shrestha, H.R., Bhattarai, T.N., Manandhar, N., Galetzka, J., Knappe, E., Pratt-Sitaula, B.,
689 Aoudia A., Bilham R., 2016. Himalayan strain reservoir inferred from limited afterslip
690 following the Gorkha earthquake. *Nature Geoscience* , 9, 533-537. doi:10.1038/ngeo2734.
691
692 Moreno, M., Melnick, D., Rosenau, M., Baez, J., Klotz, J., Oncken, O., Tassara, A., Chen, J.,
693 Bataille, K., Bevis, M., Socquet, A., Bolte, J., Vigny, C., Brooks, B., Ryder, I., Grund, V.
694 Smalley, B., Carrizo, D., Bartsch, M., Hase, H., 2012, Toward understanding tectonic control

on the Mw 8.8 2010 Maule Chile earthquake. *Earth and Planetary Science Letters*, v. 321-322, p. 152-165.

Mugnier, J.L., Huyghe, P., Gajurel, A., Upreti, B.N., Jouanne, F., 2011. Seismites in the Kathmandu valley and seismic hazard in central Himalaya. *Tectonophysics*. http://dx.doi.org/10.1016/j.tecto.2011.05.012.

Mugnier, J.L., Gajurel, A., Huyghe, P., Jouanne, F., Upreti, B.N., 2013. Structural interpretation of the great earthquakes of the last millennium in Central Himalaya. *Earth Sci. Rev*. 127, 30–47. http://dx.doi.org/10.1016/j. earscirev.2013.09.003.

Mugnier J.-L., Jouanne F., Bhattarai R., Cortes-Aranda J., Gajurel A., Leturmy P., Robert X.**,** Upreti B., Vassallo R., 2017. Segmentation of the Himalayan megathrust around the Gorkha earthquake (25 April 2015) in Nepal. *Journal of Asian Earth Sciences*.

Nábělek, J., G. Hetényi, J. Vergne, S. Sapkota, B. Kafle, M. Jiang, H. Su, J. Chen, B. S. Huang, and the Hi-CLIMB Team (2009), Underplating in the Himalaya-Tibet collision zone revealed by the Hi-CLIMB experiment, Science, 325(5946), 1371–1374, doi:10.1126/science.1167719.

Nelson K. and 26 others, 1996. Partially molten middle crust beneath southern Tibet: synthesis of project INDEPTH results. *Science,* 274, 1684-1687.

Oldham, T., 1883. A catalogue of Indian earthquakes from the earliest time to the end of 1869 AD. *Mem. Geol. Survey India* 1, 163-215.

Ostini, L., Dach, R., Meindl, M., Schaer, S., Hugentobler, U., 2008. FODITS: a new tool of the Bernese GPS software. In: Torres, J.A., Hornik, H. (Eds.), *Proceedings of EUREF 2008 Symposium*, Brussels, Belgium.

Perfettini, H., Avouac, J.-P., 2004. Postseismic relaxation driven by brittle creep: A possible mechanism to reconcile geodetic measurements and the decay rate of aftershocks, application to the Chi-Chi earthquake, Taiwan. *J. Geophys. Res*., 109, B02304, doi:10.1029/2003JB002488.

729 Rice, J. R., & Ben-Zion, Y. (1996). Slip complexity in earthquake fault models. *Proceedings of*
730 *the National Academy of Sciences USA*, *93*, 3811–3818.
731
732 Robert, X., Van Der Beek, P., Braun, J., Perry, C., Mugnier, J.L., 2011. Control of detachment
733 geometry on lateral variations in exhumation rates in the Himalaya: insights from low-
734 temperature thermochronology and numerical modeling. *J. Geophy. Res.: Solid Earth* 116, 1-
735 22. doi:10.1029/2010JB007893.
736
737 Rousset, B., Barbot, S., Avouac J.P., Hsu, Y.J., 2012. Postseismic deformation following the
738 1999 Chi-Chi earthquake, Taiwan: Implication for lower-crust rheology, *J. Geophys. Res: Solid*
739 *Earth*, 117 (B12).
740
741 Ruina, A.L., 1983. Slip instability and state variable friction laws. *J. Geophys. Res.*, 88, 10,359-
742 10,370.
743
744 Scholz, C.H., 1998. Earthquakes and friction laws. *Nature* 391, 37-42.
745
746 Szeliga, W., Hough, S., Martin, S., Bilham, R., 2010. Intensity, magnitude, location, and
747 attenuation in India for felt earthquakes since 1762. *Bull. Seismol. Soc. Am.* 100, 570-584.
748 http://dx.doi.org/10.1785/0120080329.
749
750 Wang, K., Fialko, Y., 2014. Space geodetic observations and models of postseismic
751 deformation due to the 2005 M7.6 Kashmir (Pakistan) earthquake, *J. Geophys. Res*., 119, 7306-
752 7318.
753
754 Wang, K., & Fialko, Y. (2018). Observations and modeling of coseismic and postseismic
755 deformation due to the 2015 *Mw* 7.8 Gorkha (Nepal) earthquake. *Journal of Geophysical*
756 *Research:Solid Earth*, *123*, 761–779. https://doi.org/10.1002/2017JB014620
757
758 Wessel, P., Smith , W.H.F., 1995. New version of the Generic Mapping Tools released, EOS
759 Trans. AGU, 76, 329.
760

761 Wübbena, G., 1985. Software developments for geodetic positioning with GPS using TI4100
762 code and carrier measurements. Paper Presented at 1st International Symposium on Precise
763 Positioning with the Global Positioning System, *Int. Assoc. of Geod*., Rockville, Md.
764
765 Yu, S.-B., Hsu, Y.-J., Kuo, L.-C., Chen, H.-Y., Liu, C.-C., 2003. GPS measurement of
766 postseismic deformation following the 1999 Chi-Chi, Taiwan, earthquake. *J. Geophys. Res*.,
767 108(B11), 2520, doi:10.1029/2003JB002396.
768
769 Zhao, W., Nelson, K.D., Che, J., Quo, J., Lu, D., Wu, C., Liu, X., 1993. Deep seismic reflection
770 evidence for continental underthrusting beneath southern Tibet. *Nature*, 366, 555-559.
771
772 Zhao, B., Bürgmann, R., Wang, D., Tan, K., Du, R. & Zhang, R. (2017). Dominant Controls of
773 Downdip Afterslip and Viscous Relaxation on the Postseismic Displacements Following the
774 Mw7.9 Gorkha, Nepal, Earthquake. *Journal of Geophysical Research: Solid Earth*, 122(10),
775 8376-8401. doi:10.1002/2017JB014366.
776
777
778 Captions
779
780 Graphic abstract
781 Example of observed and simulated postseismic time series and test of mechanisms controlling
782 the postseismic deformation, afterslip along the northern part of the upper flat, the ramp and the
783 flower flat of the Main Himalayan Thrust (blue) or a combination of afterslip along the northern
784 part of the upper flat and the ramp of the MHT and a viscous relaxation controlled by a low
785 viscosity body centered on the lower flat of the MHT (red). The simulated time series are
786 respectively drawn in blue and red.
787
788 Figure 1. Location of the Gorkha earthquake along the upper flat of the MHT. Dark purple for
789 ramp geometry; pink, light purple, and green for fully locked, partial coupled, and ductile MHT,
790 respectively; red for rupture zones. The rupture area is bounded by lateral ramps (Mugnier et
791 al., 2017).
792
793 Figure 2. Description of inter and co-seismic deformation used for modeling the post-seismic
794 deformation with Relax software. (a) Coupling along the Main Himalayan Thrust during the

interseismic period (before the Gorkha earthquake) (modified from Jouanne et al., 2017) and location of Gorkha earthquake indicated by yellow dash line (Grandin et al, 2015). CR indicates the location of the crustal ramp. (b) Coseismic slip distribution (adapted from Grandin et al., 2015) used as input for our numerical simulation.

Figure 3. Observed (Jouanne et al., 2017) and simulated interseismic velocities using the model proposed by Jouanne et al. (2017). Velocities are expressed in the India fixed reference frame.

Figure 4. Postseismic displacements following the Gorkha earthquake for the June 24, 2015–December 2016 period. The recorded displacements are corrected for interseismic displacements.
The rupture of the Gorkha earthquake is indicated by a blue line and the rupture of its main aftershocks, on May 12, 2016, is drawn with an orange line. The star indicates the nucleation of the Gorkha earthquake to the west of its rupture. The dashed green lines indicate the location of the Judi lineament (Kayal, 2008) that separates the main rupture zone from the nucleation area (Kumar et al., 2017) and, on the eastern side, the Gaurishankar lineament (Mugnier et al., 2017). Errors ellipses are drawn for a 95% confidence level. GNSS stations installed by our team for this study are indicated in blue and permanent GNSS stations of LDG are indicated in orange.

Figure 5. Southern components for the cGNSS station displacements, corrected from interseismic velocities and seasonal signals estimated during the period before the main shock or extrapolated for the new stations. The locations of cGNSS stations are indicated in Figure 2.

Figure 6. Eastern components for the cGNSS station displacements, corrected from interseismic velocities and seasonal signals estimated during the period before the main shock or extrapolated for the new stations. The locations of cGNSS stations are indicated in Figure 2.

Figure 7. Vertical components for the cGNSS station displacements, corrected from interseismic velocities and seasonal signals estimated during the period before the main shock or extrapolated for the new stations. We present only the time series that seem to be correctly correct for seasonal components. The locations of cGNSS stations are indicated in Figure 2.

828 Figure 8. Geometry and rheological properties considered in the numerical simulations of
829 postseismic deformation. (a) Viscous relaxation controlled by a high-fluidity body embedded
830 in a half-space characterized by low fluidity; (b) afterslip along the northern part of the upper
831 flat of the MHT, along the ramp, and along the lower flat of the MHT; and (c) viscous relaxation
832 controlled by a high-fluidity body embedded in a half-space characterized by low fluidity and
833 afterslip along the crustal ramp and along the northern part of the upper flat.
834
835 Figure 9. Search for the best solution, with the plot of the WRMS, for (a) the viscous relaxation
836 hypothesis controlled by a viscous body along the lower flat of the MHT; (b) the afterslip
837 hypothesis with (a-b)σ= 10 MPA; (c) the afterslip hypothesis with (a-b)σ= 22MPA with the
838 southern time series, (d) the afterslip hypothesis with (a-b)σ= 22MPA with the vertical time
839 series; (e) afterslip and viscous relaxation controlled by a viscous body along the lower flat of
840 the MHT with the southern time series and (f) afterslip and viscous relaxation controlled by a
841 viscous body along the lower flat of the MHT with the vertical time series .
842
843 Figure 10. Observed and simulated postseismic time series with our preferred afterslip model,
844 the afterslip & viscous relaxation model, and the viscous relaxation model. The simulated time
845 series with our preferred afterslip and afterslip & viscous relaxation models almost always
846 become conflated. Blue curve: afterslip hypothesis, red curve: afterslip and viscous relaxation
847 controlled by a viscous body along the lower flat of the MHT.
848
849 Figure 11. (a) Evolution of slip over time and space, predicted by our preferred afterslip model,
850 expressed for selected dates. The locations of the permanent GNSS stations used to constrain
851 our modeling are indicated by circles, (b) zoom of afterslip distribution after two years.
852
853 Fig. 12. Comparison between interseismic slip rate, seismic slip, and after-slip predicted after
854 6 years, supposed to be the end of postseismic deformation, along the Main Himalayan Thrust.
855 See Fig. 9 for location of the cross section.
856
857

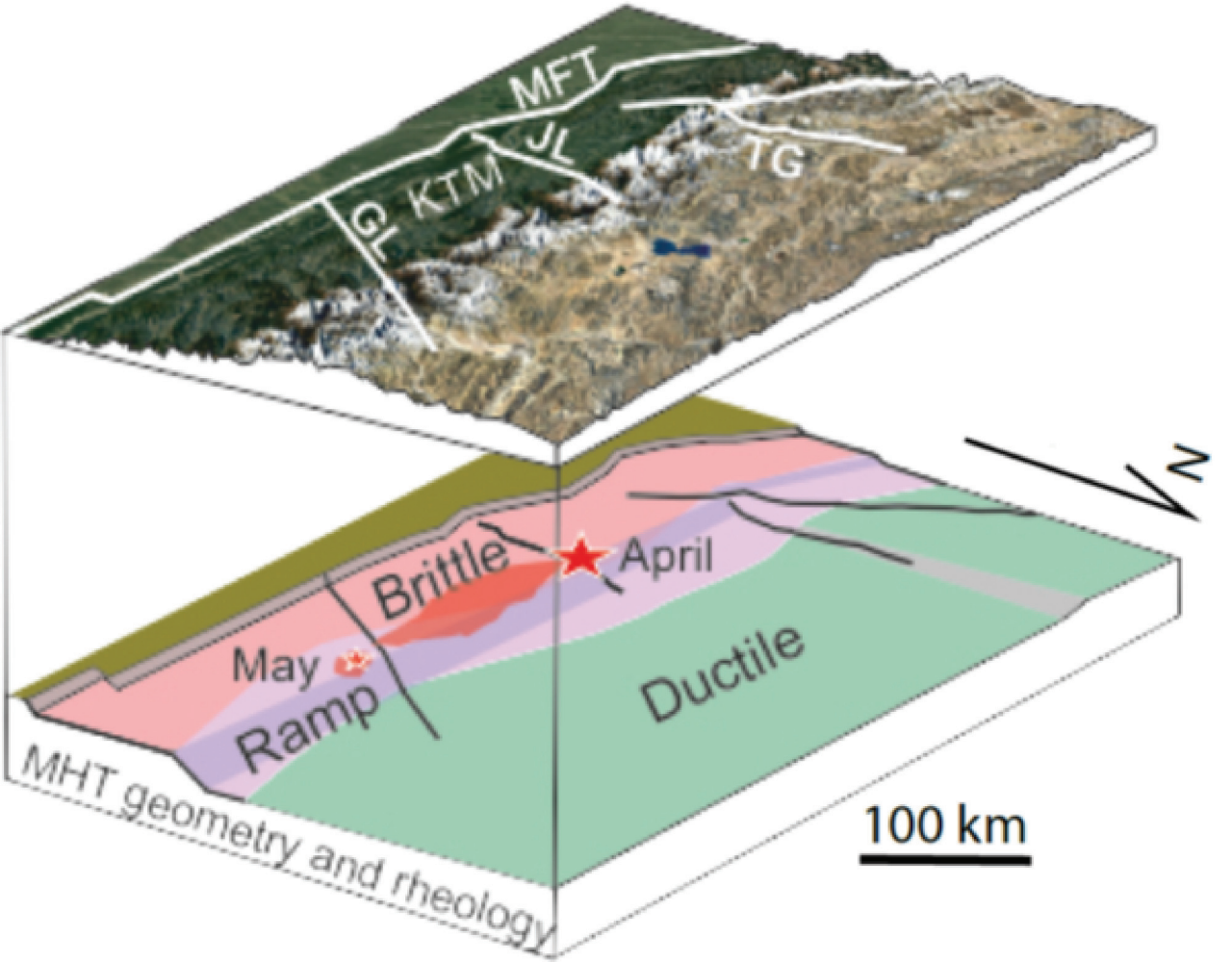
MFT
JL
KTM
GL
TG
N
Brittle
April
May
Ramp
Ductile
MHT geometry and rheology
100 km

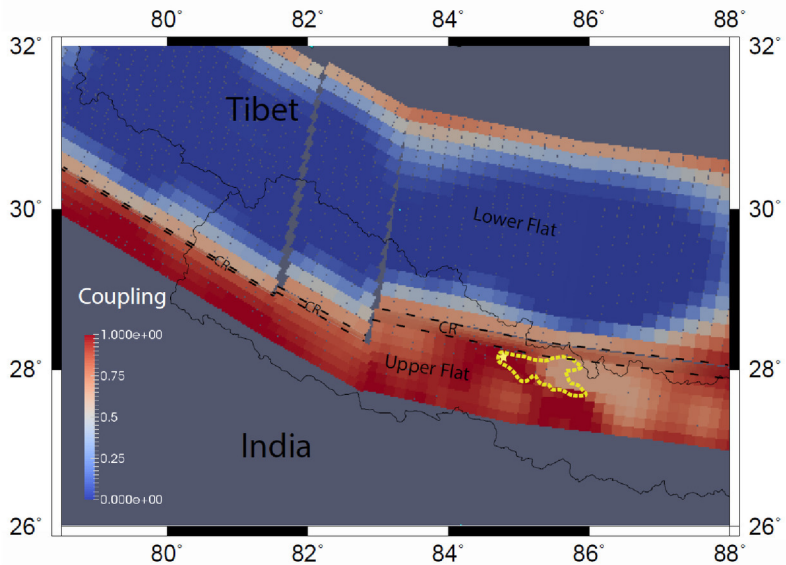
80°
82°
84°
86°
88°
32°
30°
28°
26°
Tibet
Lower Flat
Coupling
CR
Upper Flat
India
1.000e+00
0.75
0.5
0.25
0.000e+00

(a)

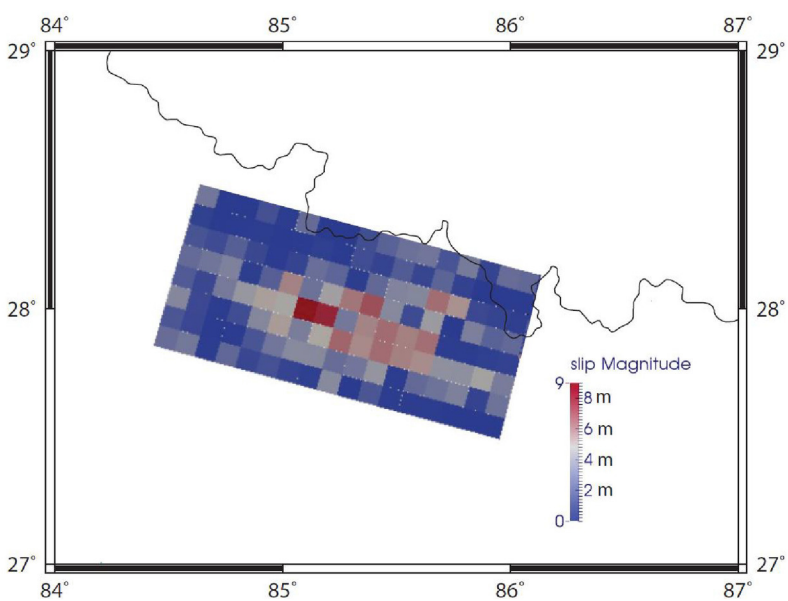
84°
85°
86°
87°
29°
28°
27°
slip Magnitude
9
8 m
6 m
4 m
2 m
0

(b)

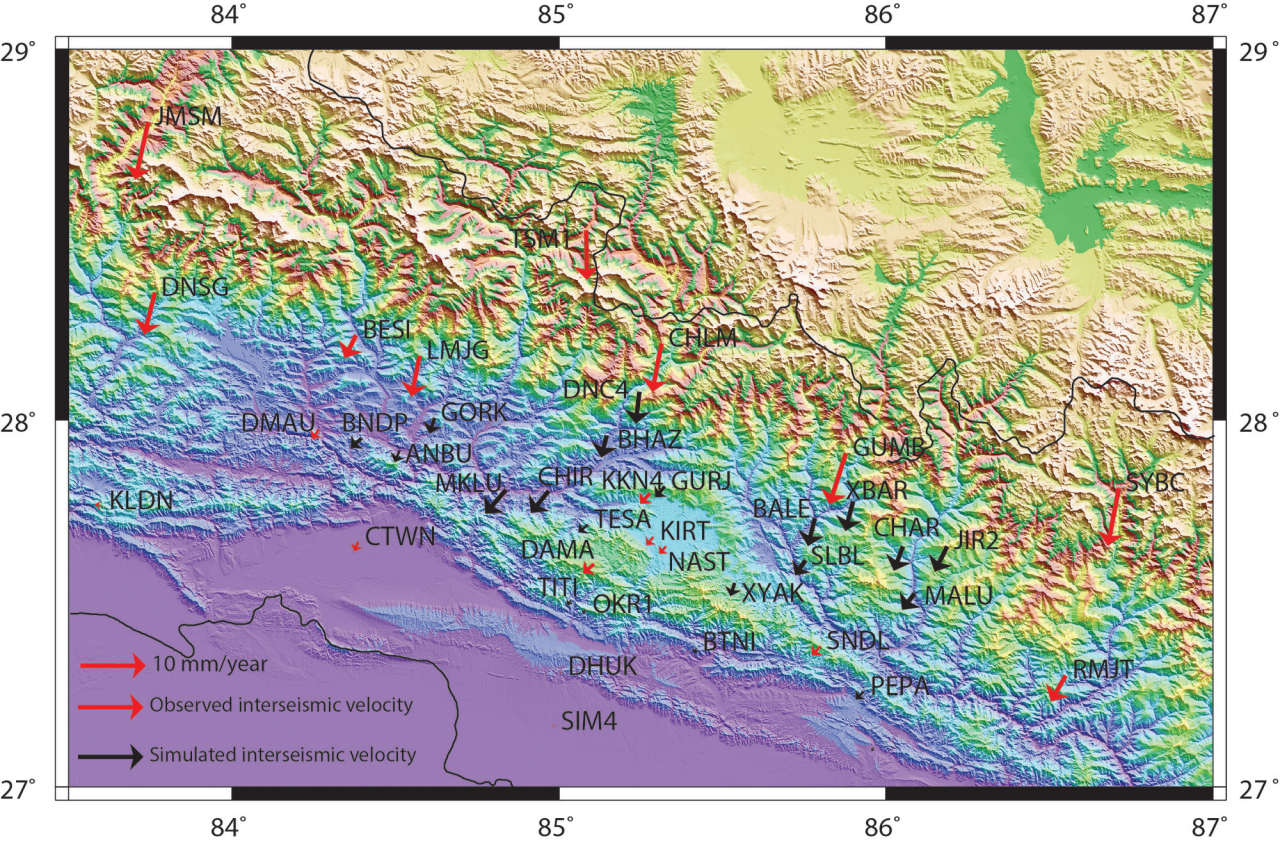
84°
85°
86°
87°
29°
28°
27°
JMSM
TSMT
DNSG
BESI
LMJG
CHLM
DNC4
GORK
DMAU
BNDP
BHAZ
ANBU
GUMP
MKLU
CHIR
KKN4
GURJ
XBAR
SYBC
KLDN
TESA
BALE
CHAR
JIR2
CTWN
KIRT
DAMA
NAST
SLBL
TITI
XYAK
MALU
OKR1
BTNI
SNDL
DHUK
RMJT
PEPA
SIM4
10 mm/year
Observed interseismic velocity
Simulated interseismic velocity

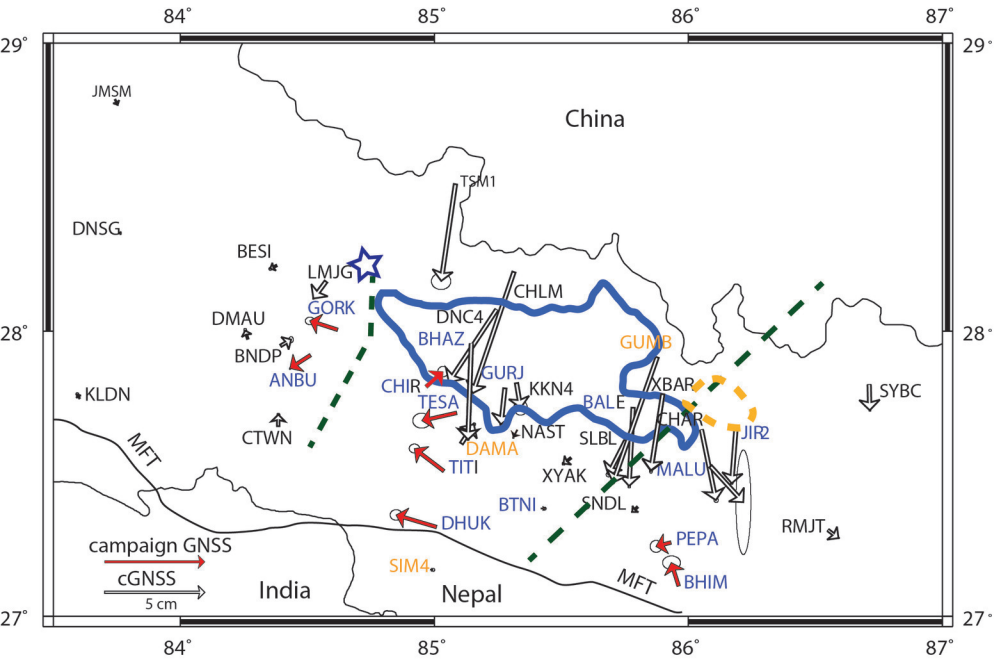
84°
85°
86°
87°
29°
28°
27°
China
India
Nepal
JMSM
TSM1
DNSG
BESI
LMJG
GORK
CHLM
DMAU
DNC4
BHAZ
GUMB
BNDP
ANBU
GURJ
CHIR
KKN4
XBAR
SYBC
KLDN
TESA
BALE
CTWN
NAST
SLBL
CHAR
JIR2
DAMA
MFT
TITI
XYAK
MALU
BTNI
SNDL
DHUK
RMJT
PEPA
SIM4
BHIM
MFT
campaign GNSS
cGNSS
5 cm

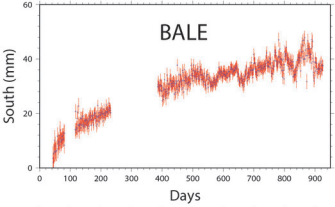
BALE
South (mm)
Days

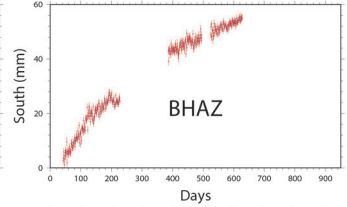
BHAZ
South (mm)
Days

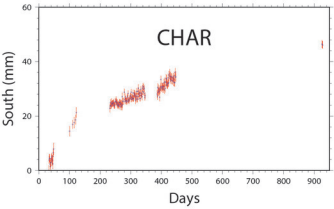
CHAR
South (mm)
Days

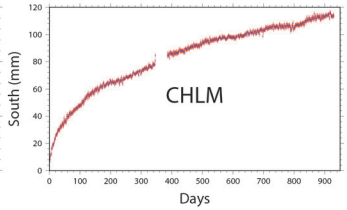
CHLM
South (mm)
Days

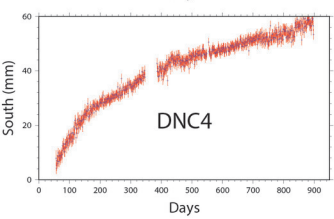
DNC4
South (mm)
Days

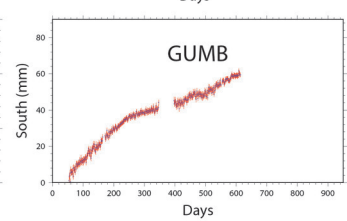
GUMB
South (mm)
Days

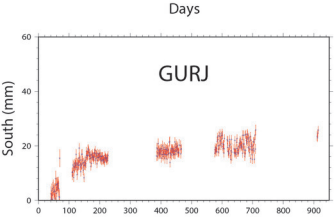
GURJ
South (mm)
Days

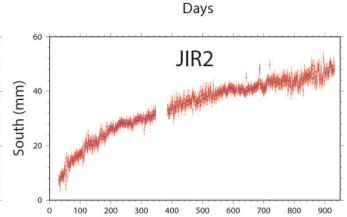
JIR2
South (mm)
Days

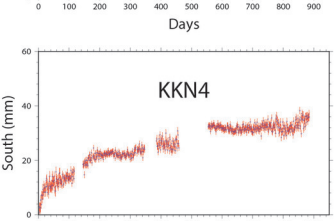
KKN4
South (mm)
Days

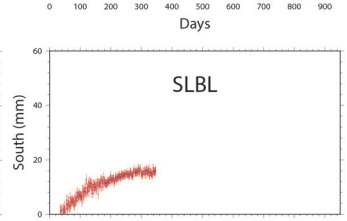
SLBL
South (mm)
Days

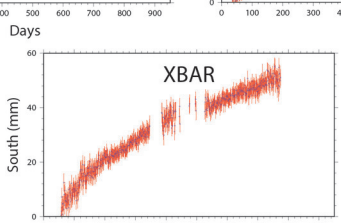
XBAR
South (mm)
Days

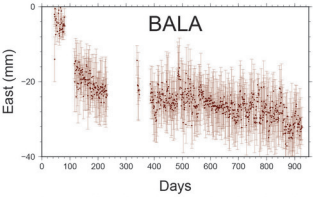
BALA
East (mm)
Days

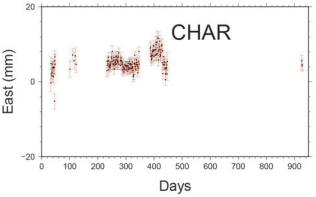
CHAR
East (mm)
Days

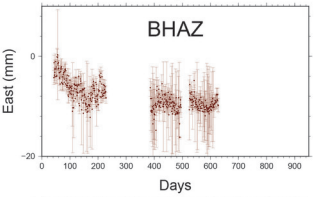
BHAZ
East (mm)
Days

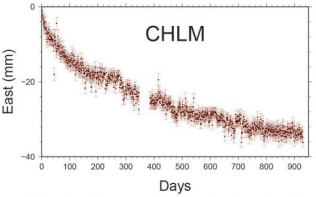
CHLM
East (mm)
Days

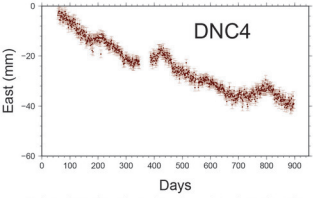
DNC4
East (mm)
Days

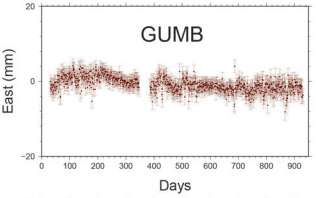
GUMB
East (mm)
Days

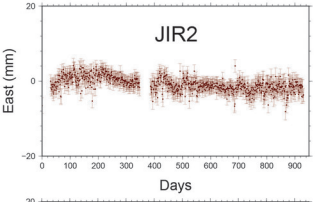
JIR2
East (mm)
Days

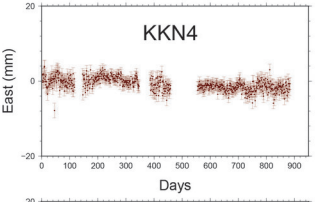
KKN4
East (mm)
Days

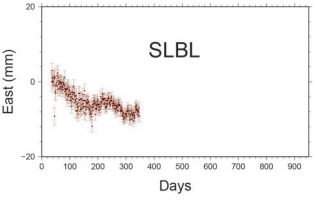
SLBL
East (mm)
Days

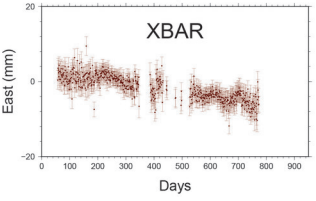
XBAR
East (mm)
Days

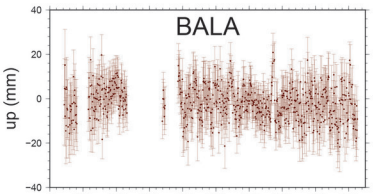
BALA
up (mm)
Days

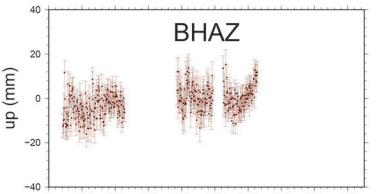
BHAZ
up (mm)
Days

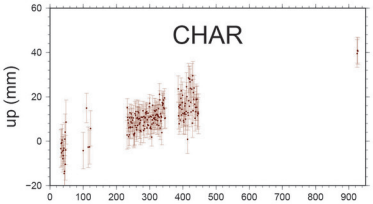
CHAR
up (mm)
Days

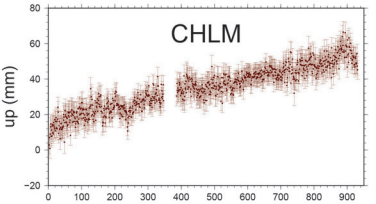
CHLM
up (mm)
Days

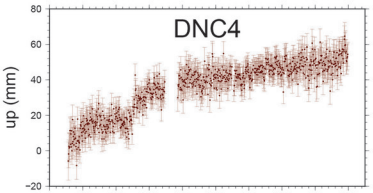
DNC4
up (mm)
Days

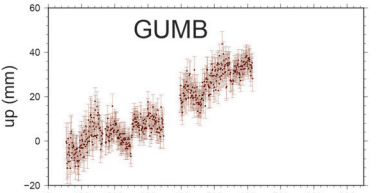
GUMB
up (mm)
Days

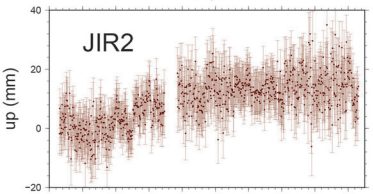
JIR2
up (mm)
Days

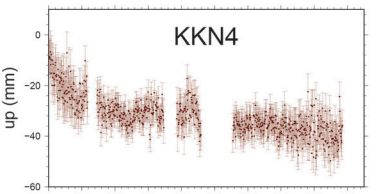
KKN4
up (mm)
Days

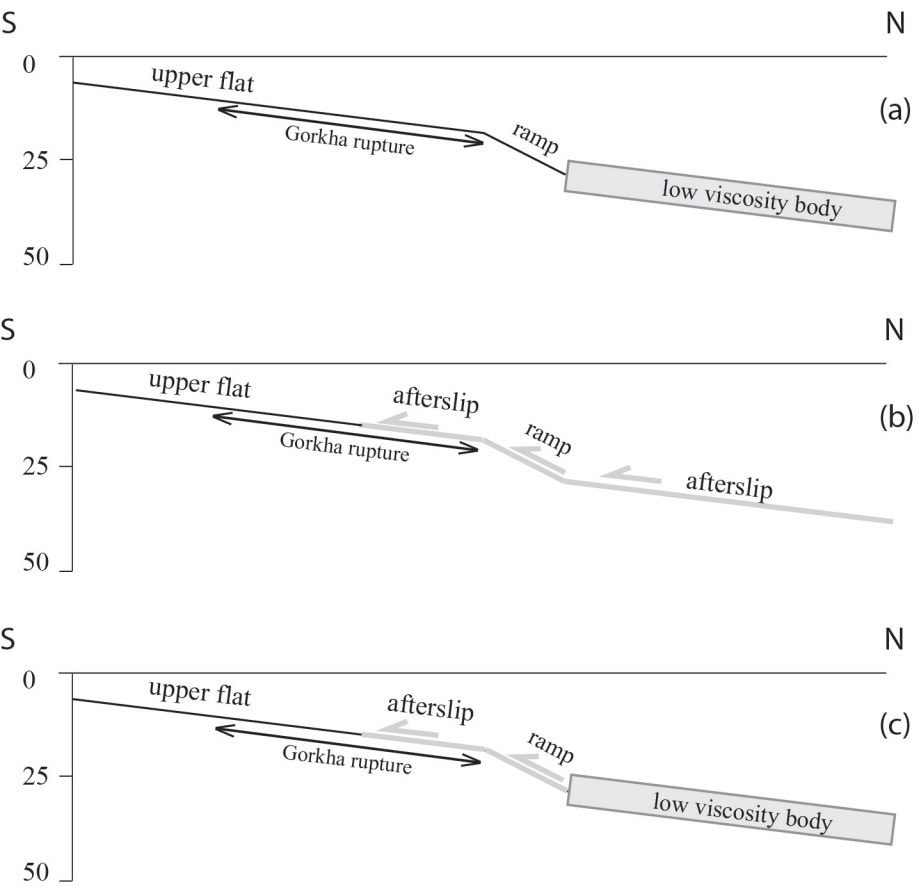
S
N
0
25
50
upper flat
Gorkha rupture
ramp
low viscosity body
(a)
S
N
0
25
50
upper flat
afterslip
Gorkha rupture
ramp
afterslip
(b)
S
N
0
25
50
upper flat
afterslip
Gorkha rupture
ramp
low viscosity body
(c)

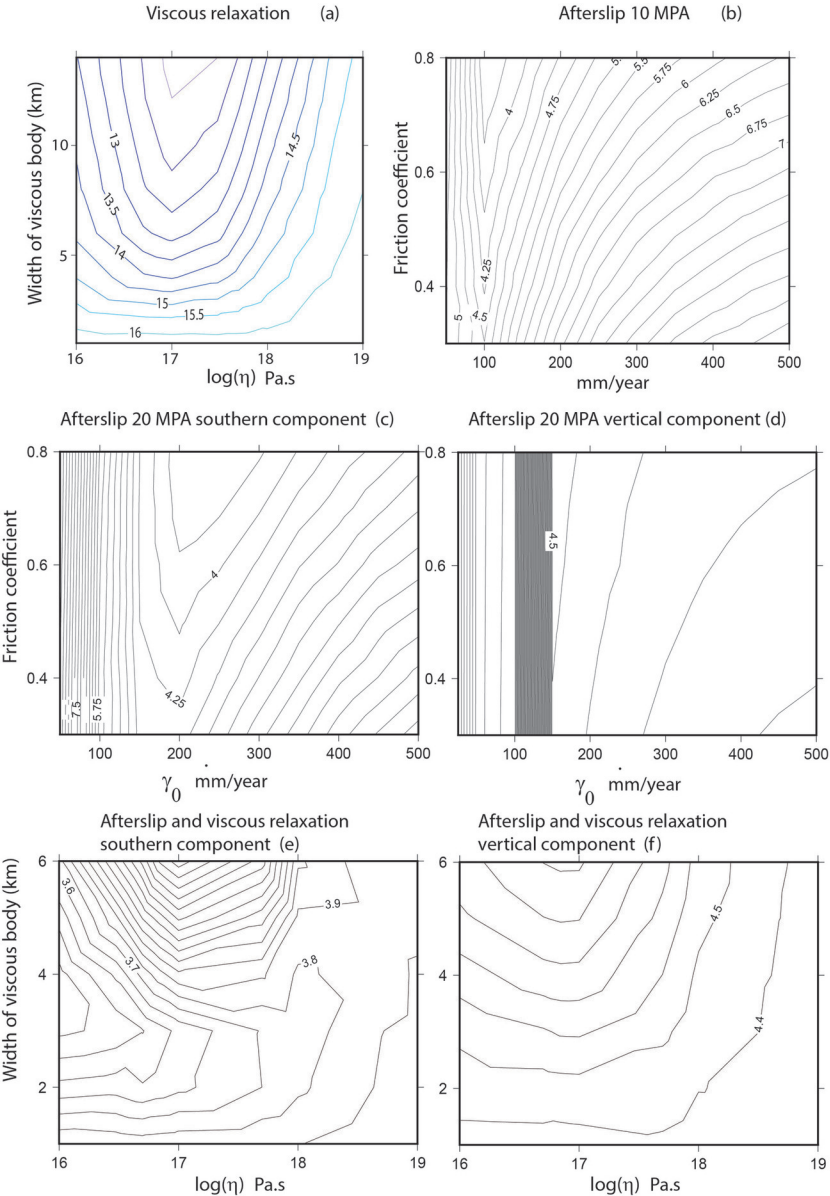
Viscous relaxation (a)
Width of viscous body (km)
log(η) Pa.s
Afterslip 10 MPA (b)
Friction coefficient
mm/year
Afterslip 20 MPA southern component (c)
Friction coefficient
$\dot{\gamma}_0$ mm/year
Afterslip 20 MPA vertical component (d)
$\dot{\gamma}_0$ mm/year
Afterslip and viscous relaxation
southern component (e)
Width of viscous body (km)
log(η) Pa.s
Afterslip and viscous relaxation
vertical component (f)
log(η) Pa.s

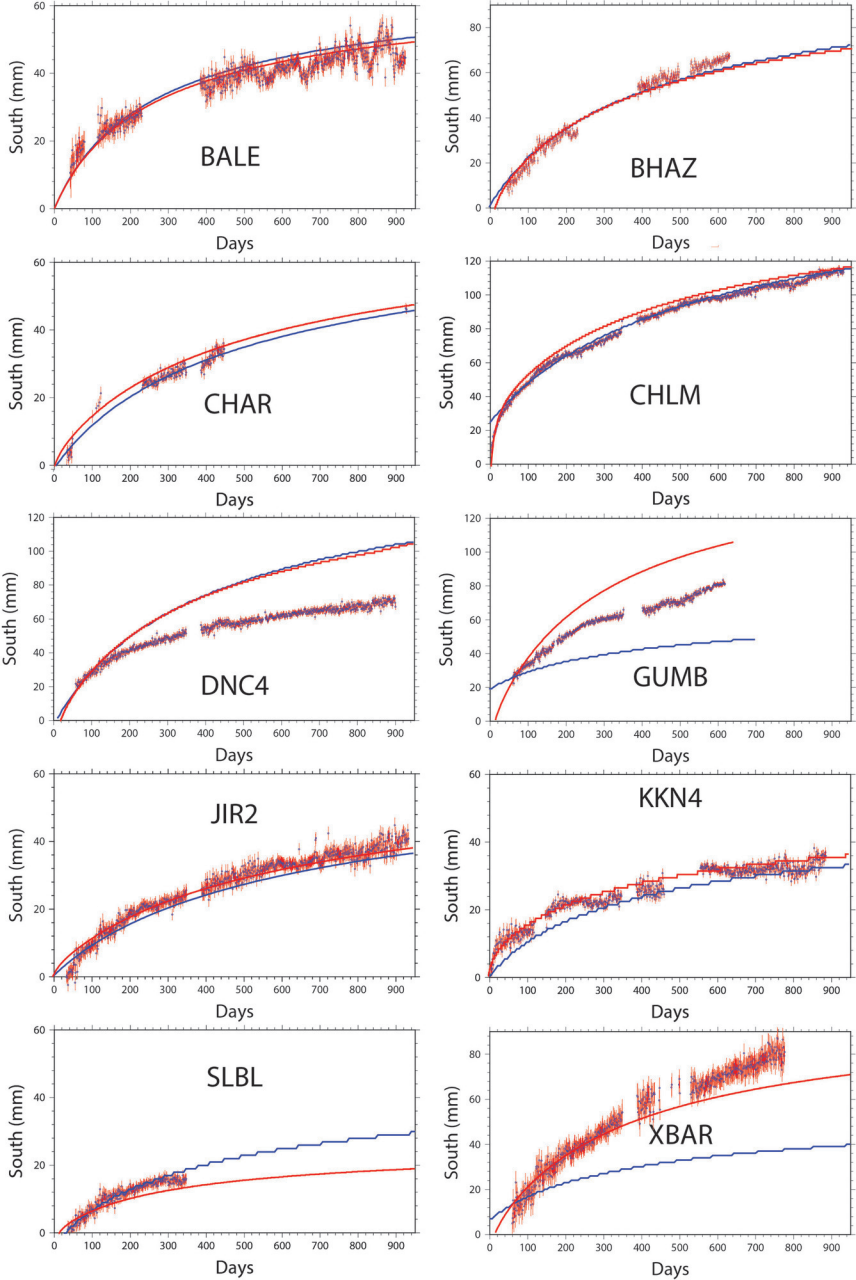
BALE
South (mm)
Days
BHAZ
South (mm)
Days
CHAR
South (mm)
Days
CHLM
South (mm)
Days
DNC4
South (mm)
Days
GUMB
South (mm)
Days
JIR2
South (mm)
Days
KKN4
South (mm)
Days
SLBL
South (mm)
Days
XBAR
South (mm)
Days

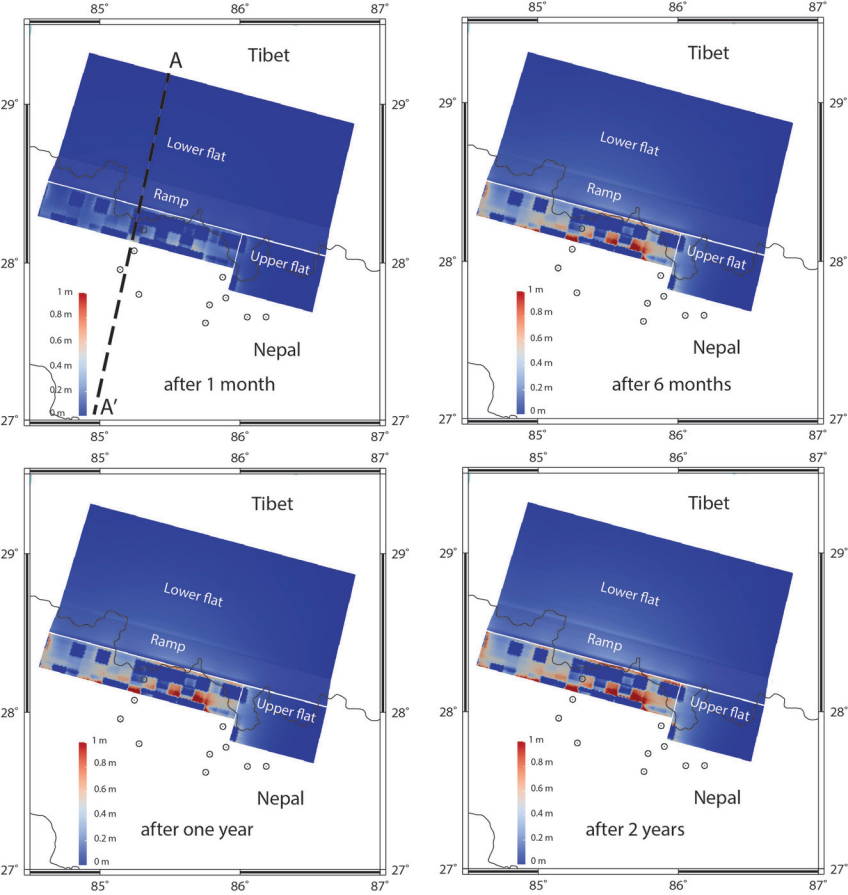
A
A′
Tibet
Lower flat
Ramp
Upper flat
Nepal
after 1 month
after 6 months
after one year
after 2 years
1 m
0.8 m
0.6 m
0.4 m
0.2 m
0 m
85°
86°
87°
29°
28°
27°

(a)

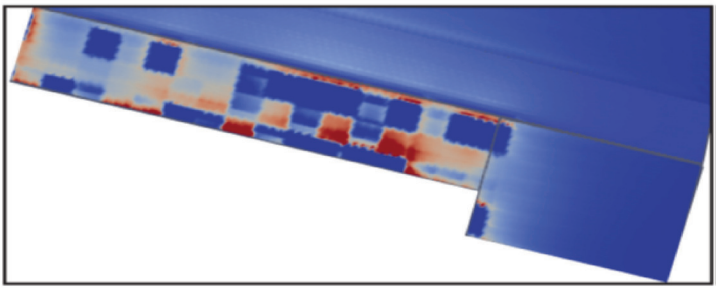

(b)

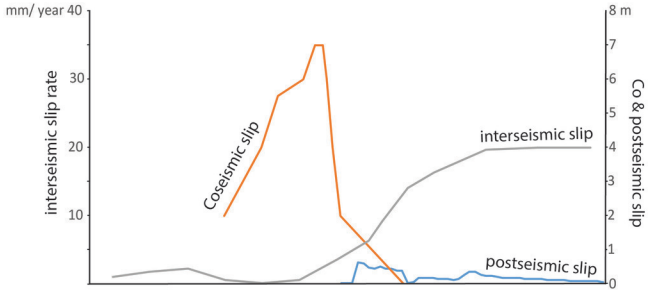
mm/ year 40
30
20
10
interseismic slip rate
8 m
7
6
5
4
3
2
1
0
Co & postseismic slip
Coseismic slip
interseismic slip
postseismic slip

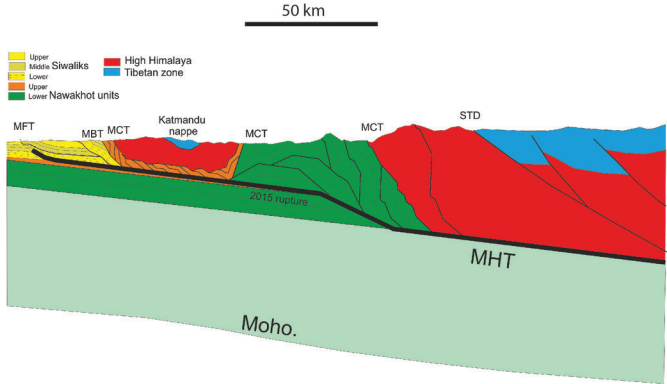
50 km
Upper
Middle Siwaliks
Lower
Upper
Lower Nawakhot units
High Himalaya
Tibetan zone
MFT
MBT
MCT
Katmandu
nappe
MCT
MCT
STD
2015 rupture
MHT
Moho.

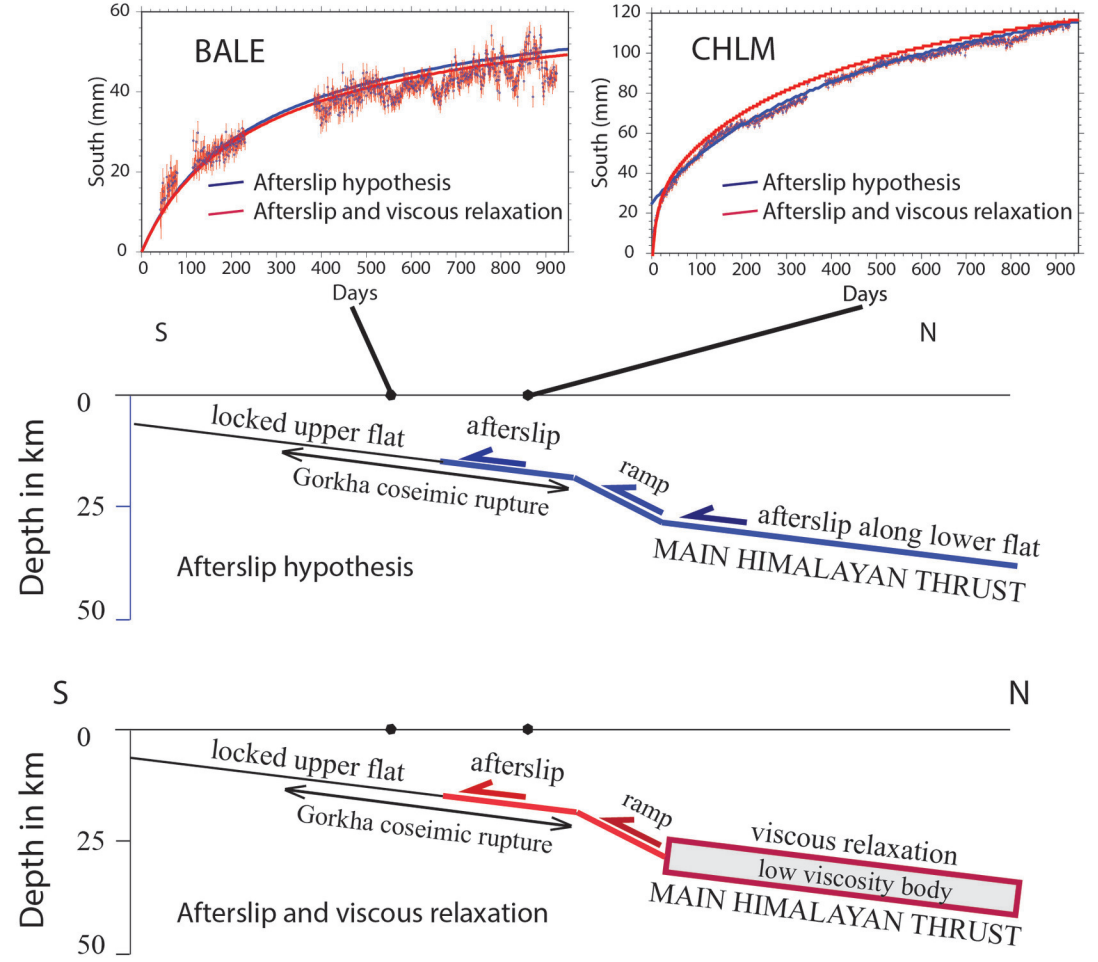
BALE
South (mm)
Days
Afterslip hypothesis
Afterslip and viscous relaxation
CHLM
South (mm)
Days
Afterslip hypothesis
Afterslip and viscous relaxation
S
N
Depth in km
locked upper flat
afterslip
Gorkha coseimic rupture
ramp
afterslip along lower flat
MAIN HIMALAYAN THRUST
Afterslip hypothesis
S
N
Depth in km
locked upper flat
afterslip
Gorkha coseimic rupture
ramp
viscous relaxation
low viscosity body
MAIN HIMALAYAN THRUST
Afterslip and viscous relaxation